

Concurrent adsorption and reduction of chromium(VI) to chromium(III) using nitrogen-doped porous carbon adsorbent derived from loofah sponge

Feng Chen¹, Shihao Guo¹, Yihao Wang¹, Lulu Ma¹, Bing Li¹, Zhimin Song (✉)¹, Lei Huang (✉)^{2,3}, Wen Zhang⁴

¹ School of Environmental and Biological Engineering, Henan University of Engineering, Zhengzhou 451191, China

² School of Environmental Science and Engineering, Guangzhou University, Guangzhou 510006, China

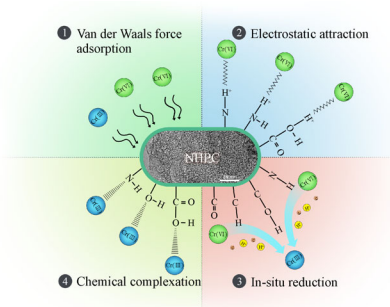
³ Guangzhou University-Linköping University Research Center on Urban Sustainable Development, Guangzhou University, Guangzhou 510006, China

⁴ John A. Reif, Jr. Department of Civil and Environmental Engineering, New Jersey Institute of Technology, Newark, NJ 07102, USA

HIGHLIGHTS

- A high-efficiency N-doped porous carbon adsorbent for Cr(VI) was synthesized.
- The maximum adsorption capacity of Cr(VI) reached up to 285.71 mg/g at 318K.
- The potential mechanism for Cr(VI) adsorption by NHPC was put forward.
- DFT analyzed the adsorption energy and interaction between NHPC and Cr(VI).

GRAPHIC ABSTRACT



ARTICLE INFO

Article history:

Received 8 May 2021

Revised 16 August 2021

Accepted 23 August 2021

Available online 15 October 2021

Keywords:

Chromium(VI)

Nitrogen-doped porous carbon

Adsorption

Reduction

Loofah sponge

ABSTRACT

To develop highly effective adsorbents for chromium removal, a nitrogen-doped biomass-derived carbon (NHPC) was synthesized via direct carbonation of loofah sponge followed by alkali activation and doping modification. NHPC possessed a hierarchical micro-/mesoporous lamellar structure with nitrogen-containing functional groups (1.33 at%), specific surface area (1792.47 m²/g), and pore volume (1.18 cm³/g). NHPC exhibited a higher Cr(VI) adsorption affinity than the HPC (without nitrogen doping) or the pristine loofah sponge carbon (LSC) did. The influence of process parameters, including pH, dosage, time, temperature, and Cr(VI) concentration, on Cr(VI) adsorption by NHPC were evaluated. The Cr(VI) adsorption kinetics matched with the pseudo-second-order model ($R^2 \geq 0.9983$). The Cr(VI) adsorption isotherm was fitted with the Langmuir isotherm model, which indicated the maximum Cr(VI) adsorption capacities: 227.27, 238.10, and 285.71 mg/g at 298K, 308K, and 318K, respectively. The model analysis also indicated that adsorption of Cr(VI) on NHPC was a spontaneous, endothermic, and entropy-increasing process. The Cr(VI) adsorption process potentially involved mixed reductive and adsorbed mechanism. Furthermore, computational chemistry calculations revealed that the adsorption energy between NHPC and Cr(VI) (−0.84 eV) was lower than that of HPC (−0.51 eV), suggesting that nitrogen doping could greatly enhance the interaction between NHPC and Cr(VI).

© Higher Education Press 2022

✉ Corresponding authors

E-mail: songzhimin1961@hotmail.com (Z. Song); huanglei@gzhu.edu.cn (L. Huang)

Special Issue—Frontier Progresses from Chinese-American Professors of Environmental Engineering and Science (Responsible Editors: Xing Xie, Jinkai Xue & Hongliang Zhang)

1 Introduction

Heavy metal contamination has aroused great concern due to its poisonous effects on the eco-systems and human health in recent years (Zhang et al., 2020c; Marciano et al., 2021). Among these heavy metals, Cr is a primary focus in wastewater treatment, due to its broad industrial processes,

for instance, metal mining, chromate manufacturing, textile industry, electroplating, and wood corrosion resistance (Zuo et al., 2020). Generally, Cr exists two steady oxidation states in a water environment, Cr(III) and Cr(VI), which may end up as different forms (e.g., Cr(OH)₄⁻, Cr(OH)₃⁰, Cr(OH)²⁺, Cr₂O₇²⁻, CrO₄²⁻, and HCrO₄⁻), depending on the aqueous temperature, pH value, oxidation-reduction potential, and Cr concentration (Nguyen et al., 2018; Yang et al., 2018). Cr(VI) is much higher toxic than Cr(III), and thus has been reported to lead to illnesses such as lung carcinoma, hepatic failure, irritability dermatosis, and gastric injury (Li et al., 2019; Li et al., 2020b; Yao et al., 2020). Therefore, effective removal techniques must be developed for Cr(VI) to protect the natural environment and ecosystems.

Different strategies have been extensively employed to dispose of Cr(VI)-containing wastewater, for example, chemical deposition, filtration, evaporation, ion exchange, electrodialysis, and membrane filtration (Nguyen et al., 2018; Yang et al., 2018). Many of these technologies for water system clean-up suffer from the intensive use of chemical reagents, high operational cost, and incomplete removal. By contrast, adsorption exhibits many fascinating features such as high efficiency, cost-effectiveness, flexibility of design, ease of operation, and environmental friendliness (Ji et al., 2021; Marciano et al., 2021; Wan et al., 2021). Selecting an affordable and practical adsorbent is critical. Biomass-derived carbon has recently been considered as ideal adsorbents for heavy metal removal from aqueous solutions, because of its inexpensive, wide availability, ease of acquisition, and mechanical and chemical stability (Xiao et al., 2019; Li et al., 2020a). Biomass-derived carbon is usually originated from biomass pyrolysis in an inert atmosphere using agricultural and industrial by-products or residues as the raw materials (Mohamed and Mahmoud, 2020; Mahmoud et al., 2021). So far, there are many different biomass materials as precursors that have been developed to adsorb Cr(VI), including sewage sludge (Nguyen et al., 2018), cassava sludge (Yang et al., 2018), coffee shells (Li et al., 2020a), *Pisum sativum* pods (Mohamed and Mahmoud, 2020), and pinewood sawdust (Yang et al., 2017).

The development of different types of biomass-derived carbon requires routine tests of adsorbent properties, adsorption kinetics, capacity, and stability or reusability. Increasing the porosities and available surface areas of carbonaceous materials could improve their adsorption abilities (Hussain et al., 2020; Li et al., 2020a). The surface functional modification of carbon materials via heteroatom dopants also improves to adsorb Cr(VI) ions (Yu et al., 2017; Li et al., 2020a; Liu et al., 2020b; Li et al., 2021). In natural waters, Cr(VI) ions primarily exist as electro-negative oxyanions (Cr₂O₇²⁻, CrO₄²⁻, and HCrO₄⁻), and thus are inclined to be adsorbed on the electropositive active sites of adsorbents (Hussain et al., 2020). Because of the electronegativity difference between C and N atoms

(2.55 and 3.04 for C and N), the incorporation of N atoms into the sp² orbitals of carbons could augment the positive electron cloud densities of the carbon skeleton through electron-withdrawal effect (Yu et al., 2017; Hussain et al., 2020; Li et al., 2020a), which potentially enhanced the electrostatic attraction of Cr(VI). Some studies demonstrated the Cr(VI) removal with N-doped carbon, such as fish scales-derived N-doped porous carbon (Yu et al., 2017), peanut hull-derived N-doped carbon spheres (Wei and Cai, 2020), copolymer-derived N-doped mesoporous carbon (Song et al., 2018), and N-doped carbon nanotube/activated carbon composites (Zhou et al., 2020). Developing facile preparation methods for N-doped biomass-derived carbon to exhibit porous structures and N-containing functional groups are crucial for increasing Cr(VI) adsorption capability and devising new adsorption mechanisms.

This study investigated a novel nitrogen-doped biomass-derived carbon (NHPC) synthesized by carbonation-alkali activation-doping modification three-step method using loofah sponge as a precursor. Loofah sponge, a full-grown fruit of loofah plants, is readily acquired, widespread, and cost-effective, making it an attractive raw material for preparing the carbonaceous adsorbents (Shih et al., 2020). The structure and properties of NHPC were tested. The batch experiments on Cr(VI) adsorption by NHPC, HPC without N-doping, and the pristine LSC without alkali activation were comparatively investigated. The relevant adsorption kinetics, isotherm, and thermodynamic analysis were performed. Furthermore, the interaction mechanism between NHPC and Cr(VI) was elucidated through the density function theory (DFT) calculation. This work aims to offer new insight for designing biomass-based adsorbents to remedy the ecological environment.

2 Materials and methods

2.1 Characterization of NHPC

Loofah sponge was obtained from Zhengzhou Botanical Garden. As shown in Fig. S1 (Section S1), the as-received loofah sponges were washed and dried, then carbonized at 400°C for 2 h under an N₂ atmosphere. Then, this carbonized sample was chemically activated with KOH (the weight ratio of KOH and the carbonized sample was 3:1) for 1.5 h at 800°C. Afterward, activated specimens were washed with hydrochloric acid to neutralize redundant KOH. The samples were washed to pH = 7. Activated samples were dried at 60°C overnight to obtain hierarchical porous biomass-derived carbon (HPC).

The obtained HPC and urea were mixed with a weight ratio of 1:0.15 in the 70 mL distilled water. The mixture was reacted in the oxidation-resistant steel autoclave at 180°C for 24 h. Finally, samples were dried at 60°C overnight, obtaining nitrogen-doped biomass-derived car-

bon (NHPC). Moreover, the loofah sponge carbon (LSC) was also pyrolyzed at 400°C for 2 h and followed at 800°C for 1.5 h without KOH activation and doping modification. The information on chemical reagents and characterization (e.g., SEM, EDS, XRD, Raman, FTIR, BET, and XPS) were detailed in the Supplementary Material (SM).

2.2 Batch adsorption experiments

The Cr(VI) solutions (50 mL) were poured into 100 mL Erlenmeyer flasks with different doses of adsorbents and the flasks oscillated on a thermostatic water circulation at 120 r/min. The Cr(VI) concentration in the filtrate was surveyed by using a UV-Vis spectrophotometer (Zhang et al., 2020a; Zhu et al., 2020). The Cr(VI) removal efficiency (η , %) and adsorption capacity (Q , mg/g) were calculated as follows (Eqs. (1) and (2)):

$$\eta = \frac{C_0 - C_t}{C_0} \times 100\%, \quad (1)$$

$$Q = \frac{(C_0 - C_t)V}{m}, \quad (2)$$

where C_0 (mg/L): the original Cr(VI) concentrations, C_t (mg/L): the remnant Cr(VI) concentrations. V (L) was the volume of Cr(VI) solution, and m (g) was the dose of adsorbent.

The detailed effects of different parameters, adsorption kinetics study, adsorption isotherm study, recycling property, and statistical analysis were displayed in the SM.

2.3 DFT calculation

The DFT calculation was carried out using version 3.0.3 of the ORCA quantum chemistry program package at the level of BLYP/def2-SVP, and the noncovalent interactions had also been quantified by Multiwfn (Liang et al., 2019; Ramirez et al., 2020). The detailed parameters of DFT calculation were displayed in the SM.

3 Results and discussion

3.1 Characterization of adsorbents

Figure 1(a) showed the surface morphology and elementary composition of NHPC. The O-rich areas and the N-rich areas overlapped the C-rich areas, suggesting that the surface of NHPC was covered by ample O- and N-containing functional groups. The KOH activation might release small amounts of gases (e.g., CO₂ and CO) that caused the pore formation (Li et al., 2011). HPC and NHPC exhibited slightly more wrinkles and open holes on the surface but were not significantly different from the morphology of LSC as shown in Fig. S2 (Section S2).

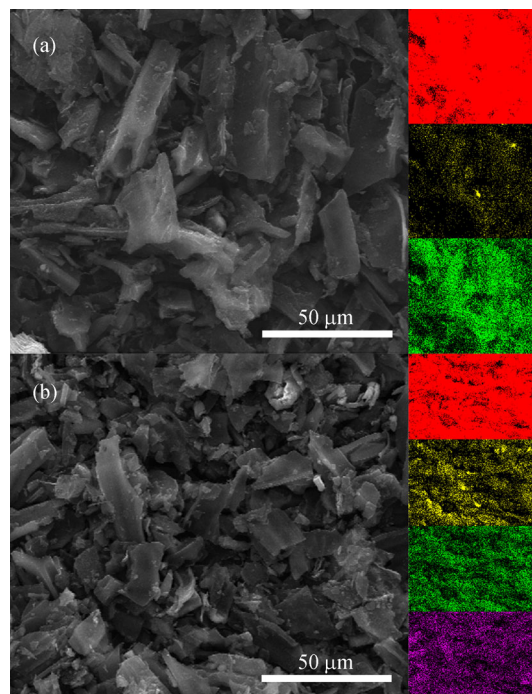


Fig. 1 SEM images and elemental maps of NHPC (a) and NHPC after Cr adsorption (b). Elemental maps of carbon (red), oxygen (yellow), nitrogen (green), and chromium (pink).

These three adsorbents all displayed a lamellar structure with a relatively slick surface and several micrometers in thickness, which was similar to other biomass-derived carbon materials (Du et al., 2021). NHPC after the Cr(VI) adsorption exhibited no significant changes to morphology as shown in Fig. 1(b), demonstrating its structural stability. The EDS elemental mapping verified the presence of Cr besides C, O, and N elements.

The XRD diffractograms of LSC, HPC, and NHPC, which all exhibited broad and weak diffraction peaks from 20° to 30° and from 40° to 45° (Fig. 2(a)). These peaks were respectively allotted to the (002) and (100) lattice planes. The relatively wide diffraction signals of NHPC manifested the state of disordered carbon between amorphous carbon and graphite (Yuan et al., 2018). Moreover, the $d_{(002)}$ spacing of HPC and NHPC were 0.3372 and 0.3378 nm, respectively, according to the Bragg equation (Zhou et al., 2016). The interlamellar spacing of NHPC was slightly larger than that of flake graphite (0.3354 nm), probably due to the N doping, which was thus easier for Cr(VI) ions to insert into the carbon frame (Yang et al., 2016).

The crystallinity and disorder degree of LSC, HPC, and NHPC were determined by the Raman spectra in Fig. 2(b). There were two characteristic peaks around 1360 cm⁻¹ (D band) and 1588 cm⁻¹ (G band). D band normally means a disordered carbon framework involved with the edge sites, pores, defects, and heteroatomic doping, while the G band

is a salient feature of the sp^2 -hybridized graphitic carbon structure (Ji et al., 2018). The integrated strength proportion of D and G bands (I_D/I_G) is adopted to assess the disorder degree of carbon materials. The I_D/I_G values for LSC, HPC, and NHPC were 1.05, 1.09, and 1.21, respectively, which indicated that more defects and disorders existed in NHPC than LSC and HPC due to the KOH chemical activation and N doping. The more defects and disorders in NHPC could offer more adsorption sites, which were favorable for the efficient and rapid removal of Cr(VI) (Sun et al., 2017).

To further examine the pore structure of LSC, HPC, and NHPC, N_2 adsorption-desorption isotherms were obtained in Fig. 2(c). The N_2 adsorption-desorption curve of LSC belonged to type I without an obvious hysteresis loop, indicative of the presence of plentiful micropores in LSC. In contrast, HPC and NHPC exhibited type I/IV N_2 adsorption isotherms, with a sharp increase tendency at low relative pressure ($P/P_0 < 0.1$) and a distinct hysteresis cycle ($P/P_0 = 0.45-1$), respectively, suggesting the coexistence of micropores and mesopores within the HPC and NHPC (Liu et al., 2020a; Jagiello et al., 2021). The pore size distributions of LSC, HPC, and NHPC in Fig. 2(d) confirmed that the LSC specimen only contained micropores between 0.7 and 2 nm, whereas HPC and NHPC possessed hierarchical micro-/mesoporous structures with

micropores' diameter ranging from 0.7 to 2.0 nm and diminutive mesopores between 2.5 and 4.0 nm.

Table 1 summarized the results of specific surface areas and pore sizes for LSC, HPC, and NHPC. The S_{BET} of NHPC was $1792.47 \text{ m}^2/\text{g}$ and was greater than those of LSC ($967.16 \text{ m}^2/\text{g}$) and HPC ($1684.34 \text{ m}^2/\text{g}$). Similarly, the specific surface area of the micropores for NHPC was also significantly greater than those of LSC or HPC. Both HPC and NHPC yielded much larger total pore volume obviously due to the chemical activation or treatment. Compared with HPC, NHPC had an increased specific surface area and decreased total pore volume. On one hand, some pores of HPC might shrink at high temperatures and pressures during the hydrothermal process (Inoue et al., 2012), on the other hand, the incorporation of N atoms into the NHPC lattice caused more structural defects and collapse of some mesoporous channels (Liu et al., 2016; Hussain et al., 2020), and leading to the number of micropores increased while the number of mesopores decreased, which then resulting in the increase of S_{BET} and the decrease of V_t for NHPC. Moreover, compared to HPC, the increase of S_{micro} and the decrease of V_{ext} for NHPC also confirmed this viewpoint. Furthermore, the S_{ext} and V_{ext} of NHPC further indicated the coexistence of microporous and small mesoporous structures of HPC or NHPC, which could offer abundant active sites and

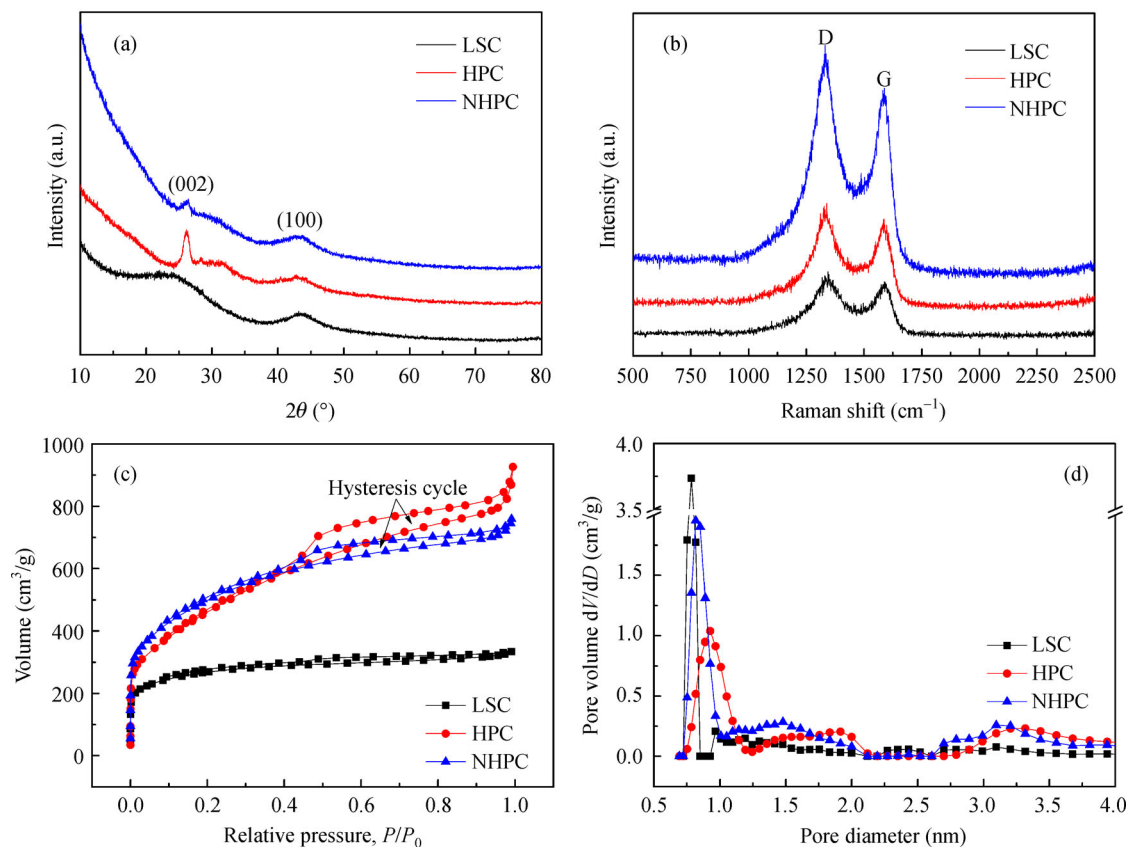


Fig. 2 The different characteristics of LSC, HPC, and NHPC (a) XRD, (b) Raman spectra, (c, d) Brunauer-Emmett-Teller.

Table 1 The textural parameters (mean values) of LSC, HPC, and NHPC

Parameters	Samples		
	LSC	HPC	NHPC
S_{BET} (m ² /g)	967.16	1684.34	1792.47
S_{micro} (m ² /g)	883.48	900.31	1342.05
S_{ext} (m ² /g)	83.68	784.03	450.42
V_{t} (cm ³ /g)	0.52	1.43	1.18
V_{micro} (cm ³ /g)	0.40	0.47	0.66
V_{ext} (cm ³ /g)	0.12	0.96	0.52
D_{ave} (nm)	2.14	3.40	2.62

Notes: S_{BET} : BET specific surface area, S_{micro} : micropores' specific surface area, S_{ext} : extra specific surface area except for micropores, V_{t} : total pore volume, V_{micro} : pore volume of micropores, V_{ext} : extra pore volume except for micropores, D_{ave} : average pore diameter.

improve the Cr(VI) adsorption ability (Hussain et al., 2020; Zhang et al., 2020b).

3.2 Comparison of adsorption characteristics

Figure S3 (Section S3) compared the adsorption efficiencies of Cr(VI) on three different types of adsorbents (LSC, HPC, and NHPC), which reached 2.7%, 49.63%, and 65.07%, respectively. Both chemically activated adsorbents (HPC and NHPC) exhibited significantly higher adsorption efficiencies than the pristine loofah sponge carbon (LSC), as the chemical activation by KOH created the larger specific surface areas and total pore volumes, which could offer plenty of active sites to arrest more Cr(VI) ions through the van der Waals force (Yang and Fox, 2018; Wang et al., 2019). NHPC achieved a higher Cr(VI) adsorption efficiency than HPC probably because the doped N enabled -N= and -NH- groups that could boost the adsorption of Cr(VI) (Wei and Cai, 2020; Ji et al., 2021; Li et al., 2021).

3.3 The assessment of pH and adsorbent dose

Figure 3(a) showed that the solution pH affected the adsorption efficiency of Cr(VI) on NHPC, which decreased with the increasing pH. The highest adsorption efficiency of 87.76% was obtained at pH 2. The pH determined the surface characteristics of NHPC and speciation of Cr(VI) in aqueous solution (Huang et al., 2017; Li et al., 2021). At low pH, the surface of NHPC became more positively charged because of the protonation of the amine and carboxylate groups (Hussain et al., 2020). As displayed in Fig. S4 (Section S4), we can see that the Zeta potential (pH_{pzc}) of NHPC was 6.3, which also confirmed that the surface of NHPC was positive at $\text{pH} < 6.3$. Different chemical species of Cr(VI) could evolve as pH changed as shown in Fig. 3(a) (Wei and Cai, 2020; Mahmoud et al., 2021). In the pH scope from 2 to 5, Cr(VI) primarily existed in the HCrO_4^- form, which thus had strong electrostatic attraction on positively charged

NHPC, leading to a good Cr(VI) adsorption efficiency under the acidic condition (Huang et al., 2017; Hussain et al., 2020). At high pH (>5), the rise of OH^- shifted the Cr(VI) species to CrO_4^{2-} and also competed or replaced the adsorption sites on NHPC. Moreover, the surface charge of NHPC became negative under the alkaline condition, which reduced the electrostatic attractions and might even switch to repulsion between NHPC and negatively charged CrO_4^{2-} . Therefore, a low adsorption efficiency (3.51%) of Cr(VI) was obtained at pH 12 (Ji et al., 2021; Mahmoud et al., 2021). The pH 2.0 was used for all the subsequent Cr(VI) batch experiments to facilitate high adsorption.

Figure 3(b) compared the effect of adsorbent dose on the Cr(VI) adsorption property. The adsorption efficiency of Cr(VI) went up from 67.33% to 87.76% with the NHPC dose increasing from 0.06 to 0.1 g/L and reached the plateau level. Accordingly, the adsorption capacity decreased with the increasing NHPC dose, because the S_{BET} or active sites were relatively excessive for the given Cr(VI) concentration of 10 mg/L (Gu et al., 2016).

3.4 Adsorption kinetics, isotherms, and thermodynamics

It was indicated that the Cr(VI) adsorption took place rapidly in the early 30 min and then reached the adsorption equilibrium at around 480 min in Fig. 3(c). The adsorption rates were found to increase slightly as the solution temperature increased with the equilibrium adsorption capacities of 90.45, 93.65, and 99.51 mg/g at 298K, 308K, and 318K, respectively. The adsorption kinetics data of Cr(VI) onto NHPC were analyzed by the pseudo-first-order and pseudo-second-order kinetics models as elaborated in Section S5. The fitting curves of relevant adsorption kinetics models were shown in Figs. S5(a) and S5(b) with the fitting parameters shown in Table S1. The squared correlation coefficients (R^2) obtained with the pseudo-second-order kinetics model (≥ 0.9983) were all greater than the pseudo-first-order kinetics model (≥ 0.8710) at 298K, 308K, and 318K respectively,

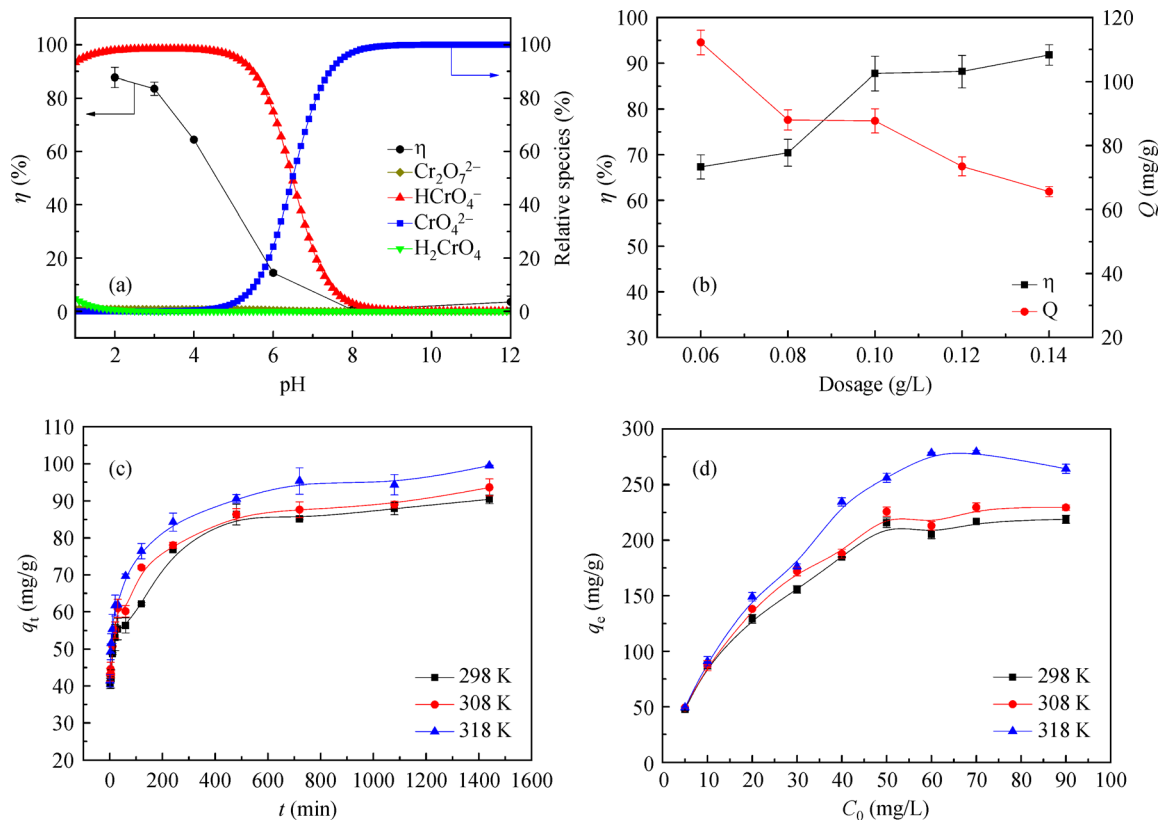


Fig. 3 (a) pH-Cr(VI) removal efficiency and the species of Cr, (b) influence of dosage, (c, d) kinetics and isotherms.

indicating that the adsorption matched well with the pseudo-second-order kinetics and was governed by a mechanism of chemisorption (Hussain et al., 2020; Zhang et al., 2020c). Thus, chemical interactions such as electron transfer, resin exchange, or electrostatic binding might occur between the various oxyanions of Cr and the radical groups (e.g., -NH- and -COOH) of NHPC (Li et al., 2020a; Ji et al., 2021; Li et al., 2021).

The adsorption capacities of Cr(VI) increased with the increase in initial Cr(VI) concentration from 5 to 50 mg/L and leveled off until more than 50 mg/L in Fig. 3(d). However, the adsorption capacities of Cr(VI) increased remarkably from approximately 200 mg/g to over 250 mg/g with increasing temperature from 298 K to 318 K, indicating that Cr(VI) adsorption by NHPC was endothermic. Furthermore, the porosity and pore volume of NHPC might also have increased at higher temperatures, which promoted Cr(VI) adsorption onto the inner pores of NHPC (Chowdhury et al., 2011). The Langmuir and Freundlich isotherm models were fitted the adsorption isotherm data in Fig. 3(d) with the fitting results shown in Figs. S5(c), S5(d), and Table S1. The Langmuir adsorption fitted the isotherms slightly better than Freundlich did, indicating that Cr(VI) adsorption on NHPC could be both monolayered and multilayered. The separation parameter R_L was between 0 and 1. Thus Cr(VI) adsorption was thermodynamically favorable (Zhang et al., 2020b). Moreover,

the fitted values of $1/n$ were far less than 1 in the Freundlich model, which also confirmed that the adsorption of Cr(VI) was thermodynamically favorable (El Nemr et al., 2021).

According to the Langmuir isotherm model, the predicted maximum adsorption capacities (q_m) of Cr(VI) onto NHPC were 227.27 mg/g (298 K), 238.10 mg/g (308 K), and 285.71 mg/g (318 K), respectively, which were comparable with or greater than the reported adsorbents as summarized in Table 2. Such as, the q_m of Cr(VI) on NHPC at 298 K was 23.1 times higher than that of cassava sludge-based activated carbon (Guo et al., 2021), and 3.1 times higher than activated carbon obtained from teakwood sawdust (Ramirez et al., 2020).

The thermodynamic parameters (ΔG° , ΔH° , and ΔS°) were calculated as detailed in Section S5 from the adsorption isotherm data (Fig. 3(d)). According to the fitting results in Table S2, ΔH° was 18.44 kJ/mol, indicating that the adsorption by using NHPC was endothermic. The positive ΔS° (66.76 J/(mol·K)) suggested the increase of randomness at solid-liquid interfaces after the Cr(VI) adsorption. The negative values of ΔG° implied that Cr(VI) adsorption process could be spontaneous. A greater negative value of ΔG° at higher temperatures (from -1.49 to -2.83 kJ/mol) suggested that Cr(VI) adsorption was more unfavorable at lower temperatures (Fazlzadeh et al., 2017).

Table 2 Summary of different adsorbents for Cr(VI) adsorption that published before

Adsorbent	Initial concentration (mg/L)	Temperature (K)	q_m (mg/g)	References
Waste peanut hull derived N-doped spherical carbons	25–250	298	181.82	Wei and Cai, 2020
Cassava sludge-based activated carbon	2–10	298	9.84	Guo et al., 2021
N/P co-doped biochars from (NH ₄) ₃ PO ₄ -pretreated coffee shells	50–300	303	223.5	Li et al., 2020a
Activated carbon obtained from teakwood sawdust	5–225	298	72.46	Ramirez et al., 2020
H ₃ PO ₄ -treated biochar	60–1050	298	116.28	Zhao et al., 2017
Nitrogen-containing activated carbon preparation from bamboo processing residues	50–280	303	185.2	Shang et al., 2014
Nitrogen-enriched activated carbon from waste medium density fiberboard	50–280	303	250	Wu et al., 2014
Nitrogen-doped hierarchical porous biomass-derived carbon	5–90	298	227.27	This work
		318	285.71	This work

3.5 Desorption and regeneration study

To assess the regeneration ability of the adsorbent, the adsorption-desorption experiments of Cr(VI) by NHPC were carried out, and the corresponding result was shown in Fig. S6. The adsorption capacity of Cr(VI) by NHPC was still higher than 88% of initial adsorption capacity after 4 adsorption-desorption recycling experiments. The decrease in the Cr(VI) adsorption capacities could be attributed to the loss of fractional reduction performance of NHPC and the unavoidable quality loss during the recycling processes. Hence, the Cr(VI) desorption and regeneration study suggested that NHPC could be repeatedly used as an economical and effective adsorbent for treating the Cr(VI)-containing wastewater.

3.6 Adsorption mechanisms

To reveal the interaction mechanisms between NHPC and Cr(VI), the surface chemical composition, and states of NHPC and NHPC-Cr were analyzed by XPS. Figure 4 showed the XPS survey spectra of NHPC confirming the presence of C 1s (284.8 eV), N 1s (400.6 eV), and O 1s (532.3 eV), which agreed well with the EDS results (Fig. 1). After the adsorption of Cr ions, two new peaks (Cr 2p) were observed at binding energies ranging from 571.0 to 595.9 eV (Wei and Cai, 2020). Figure 4(a) displayed the Cr 2p spectrum of NHPC-Cr, which consisted of two distinct energy bands for Cr 2p_{1/2} and Cr 2p_{3/2}, respectively. The peaks at 588.3 and 586.8 eV were belonged to Cr(VI) 2p_{1/2} and Cr(III) 2p_{1/2}, while those at 578.5 and 577.4 eV were assigned to Cr(VI) 2p_{3/2} and Cr(III) 2p_{3/2} (Hussain et al., 2020; Li et al., 2020c). The relative parameters of Cr in NHPC-Cr were summarized in Table S3. The NHPC surface consisted of up to 35.74% Cr(VI) and 64.26% Cr(III), which indicated that Cr(VI) could partially be changed to Cr(III) after adsorption (Li et al., 2021).

The C 1s spectra of NHPC and NHPC-Cr in Fig. 4(b) indicated the variation of carbon bonding that was further deconvoluted into four primary fitting curves with peaks at 290.3, 286.9, 285.9, and 284.8 eV corresponding to O-C=O, C=O, C-OH, and C-C/C-H, respectively (Zhang et al., 2020b; Li et al., 2021). The proportion of groups C-C/C-H reduced (from 68% to 56%), whereas the proportion of groups C-OH, C=O increased (from 10%, 6% to 25%, 12%, respectively) compared with before Cr(VI) adsorption. This was because the surface functional groups of C-C/C-H, C-OH, and C=O were expected to be involved in the reduction of the adsorbed Cr(VI) to Cr(III) as the Eqs. (3)–(5) (Jung et al., 2013; Li et al., 2021). What's more, the reaction in Eq. (6) explained the reduction of the proportion of groups O-C=O from 15.72% to 6.95%.

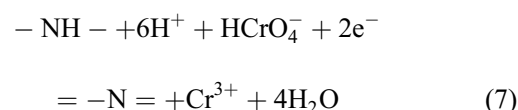
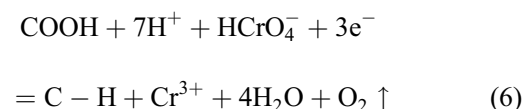
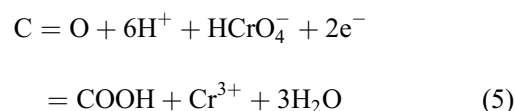
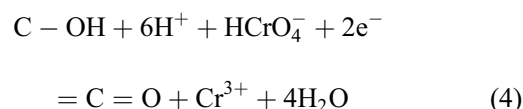
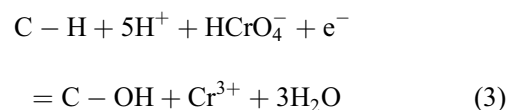


Figure 4(c) showed that the N 1s spectrum of NHPC

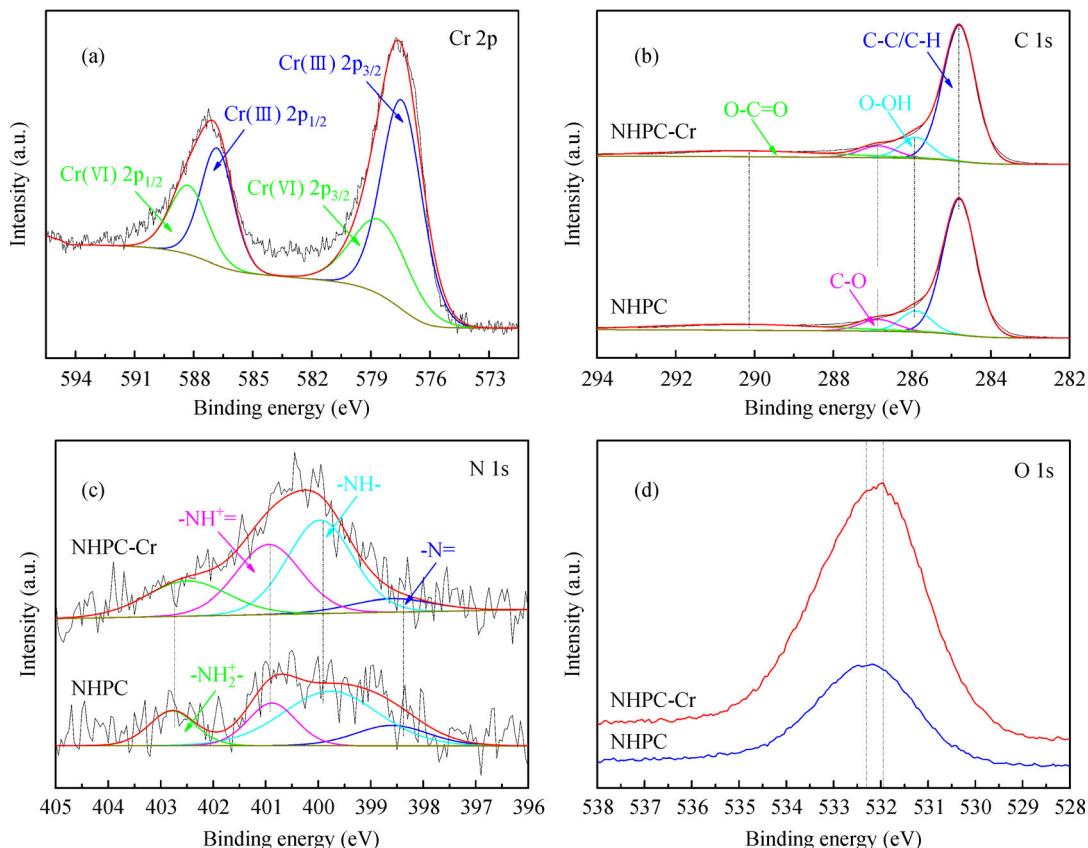


Fig. 4 The X-ray photoelectron spectroscopy: (a) Cr 2p, (b) C 1s, (c) N 1s, and (d) O 1s spectra of NHPC and NHPC-Cr.

exhibited four peaks of 402.8, 400.9, 399.8, and 398.6 eV that were assigned to -NH^+_{2-} , $\text{-NH}^+ =$, -NH- , and $\text{-N} =$, respectively (Ji et al., 2021; Li et al., 2021). After adsorbing Cr(VI), the proportion of groups -NH- decreased from 50.31% to 41.69%, probably due to the oxidation of -NH- to $\text{-N} =$ by Cr(VI) in Eq. (7) (Gao et al., 2016; Li et al., 2021). Meanwhile, the relative ratios of -NH^+_{2-} and $\text{-NH}^+ =$ increased, which was likely attributed to the incorporation of H^+ on $\text{-N} =$ (Li et al., 2021), which probably explained the decrease of $\text{-N} =$ content after the Cr(VI) adsorption. Moreover, the -NH^+_{2-} and $\text{-NH}^+ =$ groups had an electrostatic attraction toward the negatively charged HCrO_4^- (Ji et al., 2021). Table S3 indicated that the binding energies of O 1s for NHPC (532.3 eV) and NHPC-Cr (531.9 eV) were slightly different, probably due to the formation of Cr-O bonds (Ji et al., 2021).

Figure S7 showed that the pristine NHPC exhibited FTIR peaks at 1080, 1389, 1631, 2845/2919, and 3440 cm^{-1} , owing to radical groups: C-O-C, C-N, C=O/C=N, C-H, and O-H/N-H, respectively (Li et al., 2020a; Wei and Cai, 2020; Guo et al., 2021; Ji et al., 2021). The peak of 805 cm^{-1} appeared after adsorbing Cr(VI), indicating the Cr-O bonds (Zhao et al., 2017). The intensity of peaks of O-H/N-H, C-H, and C=O/C=N declined substantially after the adsorption of Cr(VI). The FTIR results implied

that Cr(III) or Cr(VI) ions combined with the O-/N-containing functional groups strongly (Ji et al., 2021; Mahmoud et al., 2021). Clearly, this interaction governed the adsorption mechanism on NHPC as illustrated in the graphic abstract, where: van der Waals force adsorption, electrostatic attraction, redox reactions, and chemical complexation might take place sequentially or concurrently as verified by the following DFT analysis.

A monolayer graphene sheet with surface pores and C=O, C-OH groups was built as the model surface to simulate the interactions of HPC, NHPC, and HCrO_4^- as illustrated in Figs. 5(a) and 5(b). Moreover, different nitrogen groups, such as graphitic N, pyrrolic N (-NH-), and pyridinic N ($\text{-N} =$), were added to represent the N doping. The adsorptive structure and energies (E_{ads}) of $\text{HPC} \cdots \text{HCrO}_4^-$ and $\text{NHPC} \cdots \text{HCrO}_4^-$ were optimized, respectively. The HCrO_4^- adsorption energy for NHPC (-0.84 eV) was much smaller than that for HPC (-0.51 eV). The value of E_{ads} was more negative, meaning that HCrO_4^- was more easily adsorbed and the $\text{NHPC} \cdots \text{HCrO}_4^-$ system was more stable (Huang and Hu, 2020). Moreover, the adsorption energies between the CrO_4^{2-} and adsorbents (HPC and NHPC) were also calculated, as shown in Fig. S8. We can see that the CrO_4^{2-} adsorption energy for NHPC (-1.06 eV) was also smaller than that for HPC

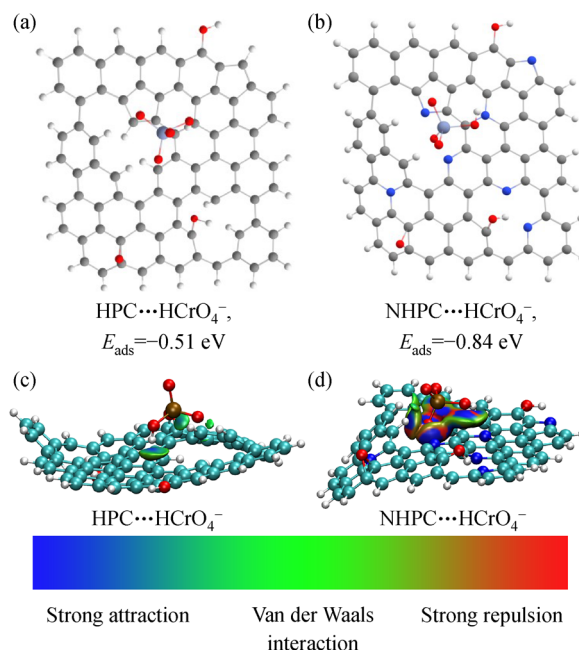


Fig. 5 The density functional calculation of HPC...HCrO₄⁻ (a, c) and NHPC...HCrO₄⁻ (b, d).

(−0.27 eV), again demonstrating the N doping could increase the interaction between Cr(VI) species and adsorbent.

Independent gradient model (IGM) analysis was then performed to interpret the different adsorption energies. IGM analysis generated the 3D isosurface graphs in Figs. 5(c) and 5(d), where the red regions indicated the strong steric exclusion in cage and ring. Green regions indicated the weak interaction of van der Waals. Blue represented the strong attractive interaction, for example, halogen-bond interaction, hydrogen-bond interaction, and electrostatic attraction (Liang et al., 2019). For HPC...HCrO₄⁻, the primary interaction was the weak interaction of van der Waals. For NHPC...HCrO₄⁻, HCrO₄⁻ and the pyridinic, pyrrolic, and graphitic N atoms underwent a strong attraction interaction, thus increasing the Cr(VI) adsorption on NHPC.

4 Conclusions

In summary, a new biomass-derived adsorbent (NHPC) was synthesized from loofah sponge and yielded a hierarchical porous structure and N-containing functional groups that led to high-efficiency adsorption of Cr(VI). The Cr(VI) adsorption process matched well with the pseudo-second-order kinetics and the Langmuir model with the maximum Cr(VI) adsorption capacities of 227.27, 238.10, and 285.71 mg/g at 298K, 308K, and 318K, respectively. The thermodynamics analysis showed that the Cr(VI) adsorption was a spontaneous, endothermic, and entropy-increasing process. The primary mechanisms

for Cr(VI) adsorption on NHPC involved van der Waals force adsorption, electrostatic attraction, in situ reduction of Cr(VI) to Cr(III), and chemical complexation. Furthermore, the computational chemistry calculations revealed that N doping could improve the binding ability between NHPC and Cr(VI). Development of this biomass-based adsorbent could pave avenues toward low-cost and environmentally friendly remediation for heavy metal removal.

Acknowledgements This work is financially funded by the National Natural Science Foundation of China (Grant No. 41872169), the Project of Education Department of Henan Province (No. 21A610002), and the Innovation and entrepreneurship training plan for college students of Henan Province in 2020 (No. S202011517004). The authors would also like to thank the workers in Shiyanjia Laboratory for the DFT calculation and language editing service.

Electronic Supplementary Material Supplementary material is available in the online version of this article at <https://doi.org/10.1007/s11783-021-1491-6> and is accessible for authorized users.

References

- Chowdhury S, Mishra R, Saha P, Kushwaha P (2011). Adsorption thermodynamics, kinetics and isosteric heat of adsorption of malachite green onto chemically modified rice husk. *Desalination*, 265(1–3): 159–168
- Du J, Zhang Y, Lv H, Chen A (2021). Silicate-assisted activation of biomass towards N-doped porous carbon sheets for supercapacitors. *Journal of Alloys and Compounds*, 853: 157091
- El Nemr A, Aboughaly R M, El Sikaily A, Ragab S, Masoud M S, Ramadan M S (2021). Utilization of sugarcane bagasse/ZnCl₂ for

- sustainable production of microporous nano-activated carbons of type I for toxic Cr(VI) removal from aqueous environment. *Biomass Conversion and Biorefinery*, doi: 10.1007/s13399-021-01445-6
- Fazlzadeh M, Khosravi R, Zarei A (2017). Green synthesis of zinc oxide nanoparticles using *Peganum harmala* seed extract, and loaded on *Peganum harmala* seed powdered activated carbon as new adsorbent for removal of Cr(VI) from aqueous solution. *Ecological Engineering*, 103: 180–190
- Gao Y, Chen C, Tan X, Xu H, Zhu K (2016). Polyaniline-modified 3D-flower-like molybdenum disulfide composite for efficient adsorption/photocatalytic reduction of Cr(VI). *Journal of Colloid and Interface Science*, 476: 62–70
- Gu H, Lou H, Ling D, Xiang B, Guo Z (2016). Polystyrene controlled growth of zerovalent nanoiron/magnetite on a sponge-like carbon matrix towards effective Cr(VI) removal from polluted water. *RSC Advances*, 6(111): 110134–110145
- Guo C, Ding L, Jin X, Zhang H, Zhang D (2021). Application of response surface methodology to optimize chromium(VI) removal from aqueous solution by cassava sludge-based activated carbon. *Journal of Environmental Chemical Engineering*, 9(1): 104785
- Huang J, Cao Y, Shao Q, Peng X, Guo Z (2017). Magnetic nanocarbon adsorbents with enhanced hexavalent chromium removal: Morphology dependence of fibrillar vs particulate structures. *Industrial & Engineering Chemistry Research*, 56(38): 10689–10701
- Huang Y, Hu H (2020). The interaction of perrhenate and acidic/basic oxygen-containing groups on biochar surface: A DFT study. *Chemical Engineering Journal*, 381: 122647
- Hussain I, Qi J, Sun X, Wang L, Li J (2020). Melamine derived nitrogen-doped carbon sheet for the efficient removal of chromium(VI). *Journal of Molecular Liquids*, 318: 114052
- Inoue T, Okuma O, Masuda K, Yasumuro M, Miura K (2012). Hydrothermal treatment of brown coal to improve the space time yield of a direct liquefaction reactor. *Energy & Fuels*, 26(4): 2198–2203
- Jagiello J, Chojnacka A, Pourhosseini S E M, Wang Z, Beguin F (2021). A dual shape pore model to analyze the gas adsorption data of hierarchical micro-mesoporous carbons. *Carbon*, 178: 113–124
- Ji Q, Hu C, Liu H, Qu J (2018). Development of nitrogen-doped carbon for selective metal ion capture. *Chemical Engineering Journal*, 350: 608–615
- Ji Y, Xu F, Zhang P, Xu Y, Zhang G (2021). Green synthesis of poly(pyrrrole methane)-based adsorbent for efficient removal of chromium (VI) from aqueous solution. *Journal of Cleaner Production*, 293: 126197
- Jung C, Heo J, Han J, Her N, Lee S J, Oh J, Ryu J, Yoon Y (2013). Hexavalent chromium removal by various adsorbents: Powdered activated carbon, chitosan, and single/multi-walled carbon nanotubes. *Separation and Purification Technology*, 106: 63–71
- Li H, Li N, Zuo P, Qu S, Shen W (2021). Efficient adsorption-reduction synergistic effects of sulfur, nitrogen and oxygen heteroatom co-doped porous carbon spheres for chromium(VI) removal. *Colloids and Surfaces A, Physicochemical and Engineering Aspects*, 618: 126502
- Li J, He F, Shen X, Hu D, Huang Q (2020a). Pyrolyzed fabrication of N/P co-doped biochars from $(\text{NH}_4)_3\text{PO}_4$ pretreated coffee shells and appraisal for remedying aqueous Cr(VI) contaminants. *Bior- esource Technology*, 315: 123840
- Li J, Yu H, Zhang X, Zhu R, Yan L (2020b). Crosslinking acrylamide with EDTA-intercalated layered double hydroxide for enhanced recovery of Cr(VI) and Congo red: Adsorptive and mechanistic study. *Frontiers of Environmental Science & Engineering*, 14(3): 52
- Li M, He J, Tang Y, Sun J, Fu H, Wan Y, Qu X, Xu Z, Zheng S (2019). Liquid phase catalytic hydrogenation reduction of Cr(VI) using highly stable and active Pd/CNT catalysts coated by N-doped carbon. *Chemosphere*, 217: 742–753
- Li X, Xing W, Zhuo S, Zhou J, Li F, Qiao S Z, Lu G Q (2011). Preparation of capacitor's electrode from sunflower seed shell. *Bioresource Technology*, 102(2): 1118–1123
- Li Z, Fan R, Hu Z, Li W, Zhou H, Kang S, Zhang Y, Zhang H, Wang G (2020c). Ethanol introduced synthesis of ultrastable 1T-MoS₂ for removal of Cr(VI). *Journal of Hazardous Materials*, 394: 122525
- Liang X, Fei Y, Xie Q, Liu Y, Lu M, Xia F, Nie Y, Ji J (2019). Sulfuryl fluoride absorption from fumigation exhaust gas by biobased solvents: thermodynamic and quantum chemical analysis. *Industrial & Engineering Chemistry Research*, 58(12): 5018–5029
- Liu B, Zhang Q, Wang Z, Li L, Jin Z, Wang C, Zhang L, Chen L, Su Z (2020a). Nitrogen and sulfur-codoped porous carbon nanospheres with hierarchical micromesoporous structures and an ultralarge pore volume for high-performance supercapacitors. *ACS Applied Materials & Interfaces*, 12(7): 8225–8232
- Liu J, Wang X, Lu Q, Yu R, Chen M, Cai S, Wang X (2016). Synthesis of nitrogen and sulfur co-doped carbon derived from chromium carbide for the high performance supercapacitor. *Journal of the Electrochemical Society*, 163(14): A2991–A2998
- Liu X, Rao L, Yao Y, Chen H (2020b). Phosphorus-doped carbon fibers as an efficient metal-free bifunctional catalyst for removing sulfamethoxazole and chromium(VI). *Chemosphere*, 246: 125783
- Mahmoud M E, Mohamed A K, Salam M A (2021). Self-decoration of N-doped graphene oxide 3-D hydrogel onto magnetic shrimp shell biochar for enhanced removal of hexavalent chromium. *Journal of Hazardous Materials*, 408: 124951
- Marciano J S, Ferreira R R, de Souza A G, Barbosa R F S, de Moura Junior A J, Rosa D S (2021). Biodegradable gelatin composite hydrogels filled with cellulose for chromium(VI) adsorption from contaminated water. *International Journal of Biological Macromolecules*, 181: 112–124
- Mohamed A K, Mahmoud M E (2020). Nanoscale *Pisum sativum* pods biochar encapsulated starch hydrogel: A novel nanosorbent for efficient chromium(VI) ions and naproxen drug removal. *Bioresource Technology*, 308: 123263
- Nguyen N T, Lee S Y, Chen S S, Nguyen N C, Chang C T, Hsiao S S, Trang L T, Kao C Y, Lin M F, Wang L (2018). Preparation of Zn-doped biochar from sewage sludge for chromium ion removal. *Journal of Nanoscience and Nanotechnology*, 18(8): 5520–5527
- Ramirez A, Ocampo R, Giraldo S, Padilla E, Flórez E, Acelas N (2020). Removal of Cr(VI) from an aqueous solution using an activated carbon obtained from teakwood sawdust: Kinetics, equilibrium, and density functional theory calculations. *Journal of Environmental Chemical Engineering*, 8(2): 103702
- Shang T X, Zhang J, Jin X J, Gao J M (2014). Study of Cr(VI) adsorption onto nitrogen-containing activated carbon preparation from bamboo processing residues. *Journal of Wood Science*, 60(3): 215–224

- Shih Y J, Dong C D, Huang Y H, Huang C P (2020). Loofah-derived activated carbon supported on nickel foam (AC/Ni) electrodes for the electro-sorption of ammonium ion from aqueous solutions. *Chemosphere*, 242: 125259
- Song Y, Wei G, Kopeć M, Rao L, Zhang Z, Gottlieb E, Wang Z, Yuan R, Ye G, Wang J, Kowalewski T, Matyjaszewski K (2018). Copolymer-templated synthesis of nitrogen-doped mesoporous carbons for enhanced adsorption of hexavalent chromium and uranium. *ACS Applied Nano Materials*, 1(6): 2536–2543
- Sun J, Zhang Z, Ji J, Dou M, Wang F (2017). Removal of Cr⁶⁺ from wastewater via adsorption with high-specific-surface-area nitrogen-doped hierarchical porous carbon derived from silkworm cocoon. *Applied Surface Science*, 405: 372–379
- Wan K, Huang L, Yan J, Ma B, Huang X, Luo Z, Zhang H, Xiao T (2021). Removal of fluoride from industrial wastewater by using different adsorbents: A review. *Science of the Total Environment*, 773: 145535
- Wang J, Zhao W, Li Z, Ding K, Jin Z (2019). Investigation on into the adsorption of Cu(II), Pb(II) and Cr(VI) on hollow mesoporous silica using microcalorimetry. *Journal of Thermal Analysis and Calorimetry*, 137(4): 1443–1450
- Wei J, Cai W (2020). One-step hydrothermal preparation of N-doped carbon spheres from peanut hull for efficient removal of Cr(VI). *Journal of Environmental Chemical Engineering*, 8(6): 104449
- Wu Y, Zhang J, Jin X J, Gao J M, Zhao Q (2014). Study of Cr(VI) adsorption onto nitrogen-enriched activated carbon from waste medium density fiberboard. *Wood Science and Technology*, 48(4): 713–725
- Xiao F, Cheng J, Cao W, Yang C, Chen J, Luo Z (2019). Removal of heavy metals from aqueous solution using chitosan-combined magnetic biochars. *Journal of Colloid and Interface Science*, 540: 579–584
- Yang J, Li C, Yang B, Kang S, Zhang Z (2018). Study on adsorption of chromium (VI) by activated carbon from cassava sludge. *IOP Conference Series: Earth and Environmental Science*, 128: 012017
- Yang K, Fox J (2018). DPF soot as an adsorbent for Cu(II), Cd(II), and Cr(VI) compared with commercial activated carbon. *Environmental Science and Pollution Research International*, 25(9): 8620–8635
- Yang K, Gao Q, Tan Y, Tian W, Qian W, Zhu L, Yang C (2016). Biomass-derived porous carbon with micropores and small mesopores for high-performance lithium-sulfur batteries. *Chemistry—A European Journal*, 22(10): 3239–3244
- Yang P, Guo D, Chen Z, Cui B, Xiao B, Liu S, Hu M (2017). Removal of Cr (VI) from aqueous solution using magnetic biochar synthesized by a single step method. *Journal of Dispersion Science and Technology*, 38(11): 1665–1674
- Yao Y, Mi N, He C, Zhang Y, Yin L, Li J, Wang W, Yang S, He H, Li S, Ni L (2020). A novel colloid composited with polyacrylate and nano ferrous sulfide and its efficiency and mechanism of removal of Cr(VI) from Water. *Journal of Hazardous Materials*, 399: 123082
- Yu F, Wang M, Huang B, Peng Q, Huang Y (2017). Acid-treatment effect on the N-doped porous carbon obtained from fish scales for Cr (VI) removal. *Chemical Papers*, 71(11): 2261–2269
- Yuan X, An N, Zhu Z, Sun H, Zheng J, Jia M, Lu C, Zhang W, Liu N (2018). Hierarchically porous nitrogen-doped carbon materials as efficient adsorbents for removal of heavy metal ions. *Process Safety and Environmental Protection*, 119: 320–329
- Zhang R, Li D, Sun J, Cui Y, Sun Y (2020a). In situ synthesis of FeS/Carbon fibers for the effective removal of Cr(VI) in aqueous solution. *Frontiers of Environmental Science & Engineering*, 14(4): 68
- Zhang T, Wei S, Waterhouse G I N, Fu L, Liu L, Shi W, Sun J, Ai S (2020b). Chromium (VI) adsorption and reduction by humic acid coated nitrogen-doped magnetic porous carbon. *Powder Technology*, 360: 55–64
- Zhang Y, Wang Y, Zhang H, Li Y, Zhang Z, Zhang W (2020c). Recycling spent lithium-ion battery as adsorbents to remove aqueous heavy metals: Adsorption kinetics, isotherms, and regeneration assessment. *Resources, Conservation and Recycling*, 156: 104688
- Zhao N, Zhao C, Lv Y, Zhang W, Du Y, Hao Z, Zhang J (2017). Adsorption and coadsorption mechanisms of Cr(VI) and organic contaminants on H₃PO₄ treated biochar. *Chemosphere*, 186: 422–429
- Zhou S, Zhang B, Liao Z, Zhou L, Yuan Y (2020). Autochthonous N-doped carbon nanotube/activated carbon composites derived from industrial paper sludge for chromate (VI) reduction in microbial fuel cells. *Science of the Total Environment*, 712: 136513
- Zhou X, Chen F, Bai T, Long B, Liao Q, Ren Y, Yang J (2016). Interconnected highly graphitic carbon nanosheets derived from wheat stalk as high performance anode materials for lithium ion batteries. *Green Chemistry*, 18(7): 2078–2088
- Zhu S, Wang S, Yang X, Tufail S, Chen C, Wang X, Shang J (2020). Green sustainable and highly efficient hematite nanoparticles modified biochar-clay granular composite for Cr(VI) removal and related mechanism. *Journal of Cleaner Production*, 276: 123009
- Zuo K, Huang X, Liu X, Gil Garcia E M, Kim J, Jain A, Chen L, Liang P, Zepeda A, Verduzco R, Lou J, Li Q (2020). A hybrid metal-organic framework-reduced graphene oxide nanomaterial for selective removal of chromate from water in an electrochemical process. *Environmental Science & Technology*, 54(20): 13322–13332